Enhancement of focusing properties by interfering spatial bending beams

2016 EPL 116 55002

(http://iopscience.iop.org/0295-5075/116/5/55002)

A Letters Journal Exploring the Frontiers of Physics

December 2016

EPL, **116** (2016) 55002 www.epljournal.org
doi: 10.1209/0295-5075/116/55002

Enhancement of focusing properties by interfering spatial bending beams

Hui Li[1,2], Yongzheng Xu[1], Yu Qu[1], Bin Zhang[2], Li Wang[1] and Zhongyue Zhang[1(a)]

[1] *School of Physics and Information Technology, Shaanxi Normal University - Xi'an 710062, China*
[2] *Division of public infrastructure, De-hong Vocational College - Mang-shi 678400, China*

received 7 December 2016; accepted in final form 10 January 2017
published online 1 February 2017

PACS 52.40.-w – Plasma interactions (nonlaser)
PACS 52.25.Fi – Transport properties
PACS 52.35.Hr – Electromagnetic waves (*e.g.*, electron-cyclotron, Whistler, Bernstein, upper hybrid, lower hybrid)

Abstract – In this study, two slits were designed symmetrically on a metal film to excite surface plasmon polaritons (SPPs), and two groups of parallel dielectric rectangles were designed over a metal film to convert the SPPs into double mirror-symmetric spatial bending beams. The high-energy far-field focused beams were achieved by interfering double mirror-symmetric spatial bending beams using the finite-element method The focusing properties of the proposed structure are enhanced compared with the conventional metal grating structures. Furthermore, the effects of the structural parameters on the focusing properties were investigated Results show that the focusing properties of the proposed structure rely on the structural parameters of dielectric rectangles and on the distance between the dielectric rectangles and the metal film. The position of the focusing spot relies on the distance between two slits. These findings can be applied in the fields of biology imaging, nanolithography, optical data storage and photo-biomedical detection.

Introduction. – Surface plasmon polariton (SPP) waves are surface electromagnetic waves that consist of collective electron oscillations in metal-dielectric interface decay; thus, their diffraction limits can be surpassed [1,2], thereby offering important applications in the fields of photonics and electronics [3]. Focusing beams, a type of special light waves, have increasingly attracted attention because of their potential applications in biology imaging [4], nanolithography [5], optical data storage [6], and photobiomedical detection [7,8].

Various studies on focusing beams have been reported over the past several decades. For example, the plasmonic lens, which consists of an array of nanoscale slits [9–12] or annular slits [13,14] in metallic film was proposed to achieve far-field focused beams. These nanoscale slits were designed to excite the SPP waves. These nanoscale slits, a group with a metal-insulator-metal structure, were introduced to generate a phase delay [11,12]. The phase delay depends strongly on the width and depth of the slits [11,12,14]. Structures on the metallic film, such as circular surface gratings [15], intersecting surface gratings [16–18], circular coupler based on intersecting slit arrays [19,20] or F-shaped slit arrays [21], were proposed to achieve near-field focused beams The excitation of the near-field focused beams, which are plasmonic hot spots on the surface of a metal film, can be applied in the field of sensing, manipulation and optical tweezers [22]. Studies were conducted to achieve the near-field or low-energy far-field focused beams. To achieve high-energy far-field focused beams with super-resolution remains a challenge.

Recently, high-energy far-field focused beams were achieved through interference of a double parallel Airy beam [23–25]. The Airy beam is a special wave that accelerates along parabolic trajectories and exhibits self-healing properties. The Airy beam was demonstrated by a nanoscale phase modulator on a metal film [26–30]. The dynamic controlling position [31–33] and types of polarizations [34] of the focusing spot of the far-field focused beams were also shown. However, the area of the focusing spot was smaller, and the depth of focus (DOF the distance between the two points with intensity of the maximum focal intensity at both sides [13]) was only approximately 7 μm [23]. In certain applications, such as manipulation of particles and transmission of signals among on-chip

(a) E-mail: zyzhang@snnu.edu.cn

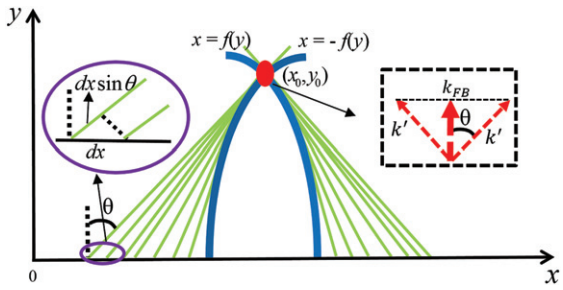

Fig. 1: (Colour online) Schematically the focusing beam is achieved by interfering double mirror-symmetric spatial bending beams. The left illustration (violet ellipse) represents the relationship between spatial bending trajectory $f(y)$ and the tangent lines. The right illustration (black rectangle) represents the relationship of wave vectors, where k' and k_{FB} represent the wave vector of the spatial bending beam and the generated focusing beam, respectively.

devices, increasing the area of the focusing spot or increasing the DOF is desirable.

In this study, two slits were designed on a metal film to excite the SPPs, and two groups of parallel dielectric rectangles were designed over a metal film to convert SPPs into double mirror-symmetric spatial bending beams. The high-energy far-field focused beams were achieved by interfering double mirror-symmetric spatial bending beams using the finite-element method. Compared with the DOF of the conventional metal grating structures, the DOF of the proposed structure was increased. Furthermore, the effects of the structural parameters on the DOF were investigated. Results show that the DOF of the proposed structure relies on the structural parameters of the dielectric rectangles and on the distance between the dielectric rectangles and metal film. The position of the focusing spot relies on the distance between the two slits. These findings have deep implications on various focus-based applications.

Theoretical analysis and structure. – Focusing beams are a result of the interference between the transverse acceleration, and the non-diffraction of double mirror-symmetric spatial bending beams. The interference process is schematically shown in fig. 1. Two mirror-symmetric spatial bending beams (dark blue curves $x = f(y)$ and $x = -f(y)$) were launched from the x plane. The mirror-symmetric spatial bending beams were superposed along the direction of propagation $(+y)$. The focusing beam (red circle) was created around the position of $(x_0,\ y_0)$. The left illustration (violet ellipse) represents the relationship between the spatial bending trajectory $f(y)$ and the tangent lines in fig. 1. The right illustration (black rectangle) represents the relationship between the wave vectors, $k_{FB} = k' \cos\theta$ in fig. 1, where k' and k_{FB} represent the wave vectors of the spatial bending beam and the generated focusing beam, respectively. θ is the half-angle between the directions of propagation of the double spatial bending beams.

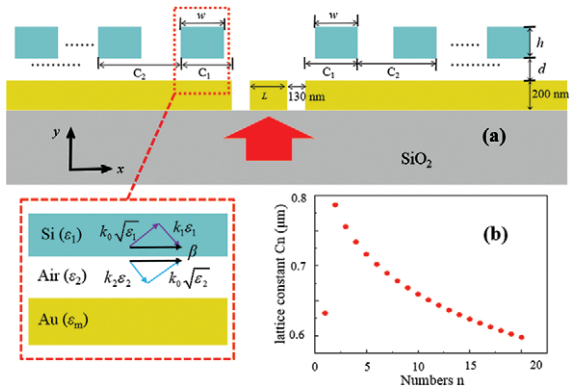

Fig. 2: (Colour online) (a) The configuration of the proposed (dielectric-air-metal) structure. The red block diagram illustrates a single dielectric rectangle above the Au/SiO_2 substrate and the relationship of structural parameters, where ε_1, ε_2 and ε_m represent the relative permittivity of Si, air and the gold film, respectively; the three sides of the triangle rectangle represent $k_{1(2m)}\varepsilon_{1(2m)}$, $k_0(\varepsilon_{1(2m)})^{0.5}$ and β. (b) Calculated local lattice constant C_n of a side of dielectric rectangles.

The configuration of the dielectric rectangles on an Au/SiO_2 substrate is shown in fig. 2(a). Two slits were symmetrically designed on the metal film, and the distance between the two slits L is presented. Two groups of parallel dielectric rectangles were symmetrically designed over the Au/SiO_2 substrate. The number of dielectric rectangles at either side of the slit is 20. The thickness and the width of the slit are fixed at 200 nm and 130 nm, respectively. w and h are the width and the height of the dielectric rectangle, and d is the distance between the rectangles and the interface of the gold film. The inset (red block) diagram illustrates a single dielectric rectangle above the Au/SiO_2 substrate, and the relationship of the structural parameters. In this work, the propagation properties of the focused beams were simulated by a two-dimensional radio frequency module of COMSOL Multiphysics software. A plane wave with 0.98 μm wavelength, magnitude of 1 v/m, and polarization in the x-direction, is incident $(+y)$ onto the slit. The relative permittivity ε_m of the gold film is $-36.4 + 3.26i$ at 0.98 μm [34]. The dielectric rectangles are silicon with a refractive index of 3.476 [35].

SPPs excited in two slits propagate along the interface of the gold film. The wave vector of SPPs is $k_{spp} = k_0\sqrt{\varepsilon_2\varepsilon_m/(\varepsilon_2+\varepsilon_m)}$, where k_0 represents the free-space wave vector, and ε_2 and ε_m represent the relative permittivity of the air and the gold film, respectively. The dielectric rectangle can be considered as a group of nano-scatterers, and the phase contribution of the n-th dielectric rectangle can be deduced as [36]

$$\varphi_n(x) = \varphi_0 + k_{spp}x - n\left(k_{spp}w - \beta w\right) - 2n\pi, \qquad (1)$$

where n is an integer, and φ_0 is the initial phase, and x is the distance of the n-th dielectric rectangles from two slits, and 2π is an additional phase difference between neighboring dielectric rectangles. The space between rectangle and

film can be considered as dielectric/air/metal ($\varepsilon_1/\varepsilon_2/\varepsilon_m$) structure. The transverse magnetic mode of this structure follows the specific dispersion relationship [37]

$$\tanh(k_2\varepsilon_2 d) = -\frac{k_1 k_2 + k_2 k_m}{k_2^2 + k_1 k_m}, \tag{2}$$

where d is the distance between dielectric rectangles and metal film, and $k_{1(2m)} = \sqrt{\beta^2 - \varepsilon_{1(2m)} k_0^2}/\varepsilon_{1(2m)}$. The effective mode index of SPPs ($n_{eff} = \beta/k_0$) is changed for different distances between dielectric rectangles and metal film. Hence, βw being a dynamic of the variation of the additional phase of SPPs propagating between the rectangle and the film is obtained. β represents the wave vector of SPPs propagating between the rectangle and the film.

The phase $\phi(x)$ of the required spatial bending beams was calculated utilizing the Legendre transform method [25,38–40]. The geometric relationship among the phase, the angle θ, and the desired arbitrary bending trajectory $f(y)$ is defined in fig. 1 (left illustration (violet ellipse)). The spatial phase can be obtained for paraxial and non-paraxial regimes [38–40],

$$\phi(x) = -\int k_0 \tan\theta \mathrm{d}x \tag{3}$$

and

$$\phi(x) = -\int k_0 \tan\theta / \sqrt{1 + \tan^2\theta} \mathrm{d}x, \tag{4}$$

where $\tan\theta = f'(y)$, $f'(y)$ is the first-order derivative of $f(y)$. The location of every dielectric rectangle can be calculated by solving the equation $\varphi_n(x) = \phi(x)$.

Results and discussion. – Under the paraxial approximation, for the curve of $f(y) = -ay^2$ (a is constant), the required phase profile $\phi(x) = -1.33 k_0 a x^{1.5}$ is obtained by applying eq. (3), where k_0 is the wave vector of light in free space, and the constant a is equal to 7×10^{-2}. The distance between every dielectric rectangle ($C_n = x_n - x_{n-1}$) is calculated (fig. 2(b)) when the number of dielectric rectangles is equal to 20. The distance C_n decreases as the distance of the dielectric rectangles from the silt increases, except in the case of the first dielectric rectangle.

The intensity distribution of the electric field ($w = 320\,\mathrm{nm}$, $h = 110\,\mathrm{nm}$, $L = 3.0\,\mu\mathrm{m}$) when the number of dielectric rectangles is equal to 20 is depicted in fig. 3(a). The distance between a rectangle and the interface of the gold film is set as 60 nm. The two mirror-symmetrical spatial bending beams propagate along the desired trajectory, and then focus on the desired spot by interfering. The transverse intensity distributions at different distances ($y = 15$, 25, and $35\,\mu\mathrm{m}$) are shown in fig. 3(b). The surface current density distributions in the x-y plane are also presented in fig. 3(c). These results demonstrate that the far-field focused beams are achieved by interfering double mirror-symmetrical spatial bending beams.

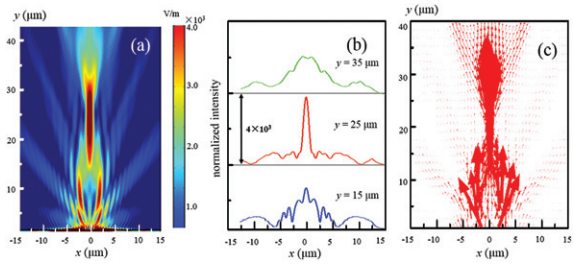

Fig. 3: (Colour online) (a) Simulation electric-field intensity distribution of the required focusing beam. (b) Transverse intensity distributions at different distances: $y = 15\,\mu$m, $25\,\mu$m, and $35\,\mu$m. (c) Distributions of surface current density in the x-y plane.

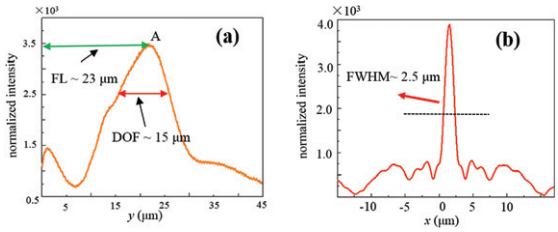

Fig. 4: (Colour online) (a) Electric-field intensity profiles of the proposed structure in the y-direction, (b) Intensity profiles of the focal spot with the proposed structure.

Figure 4(a) shows the calculated values of the DOF ($\sim 15\,\mu$m) and the focal length (FL $\sim 23\,\mu$m). The FL was defined as the distance from the dielectric-air-metal structure interface to the focal spot [13]. Figure 4(b) shows the value of the full width at half-maximum (FWHM $\sim 2.5\,\mu$m). The DOF of the proposed structure is two times longer than that of the conventional structures (*i.e.*, $15\,\mu$m *vs.* $7\,\mu$m) [23]. The FL and FWHM of the proposed structure are also longer than that of the conventional structures [23]. These results confirm that the focused beams are enhanced in the proposed structure compared with that in the conventional metal grating structures.

The DOF is associated with the number of focuses along the propagation direction, the decay length of the focused beam multiplied, the half-angle between the directions of propagation of the double spatial bending beams, and the wave vectors [16,18]. Their relationship can be simply expressed as

$$\mathrm{DOF} \propto \frac{\Im\{k'\}}{\Re\{k_{FB}\}} \cdot S(w \cdot h \cdot d) \cdot \cos\theta \ (0^\circ \le \theta < 90^\circ), \tag{5}$$

where $\Re\{k_{FB}\}$ and $\Im\{k'\}$ are functions of the wave vectors k_{FB} and k', θ is the half-angle between the directions of propagation of the double spatial bending beams, and $S(w \cdot h \cdot d)$ represents the scattering of the dielectric rectangles. The scattering of the dielectric rectangles relies on the structural parameters of dielectric rectangles and on the distance between the dielectric rectangles and metal film [36]. Evidently, eq. (5) shows that as the angle θ

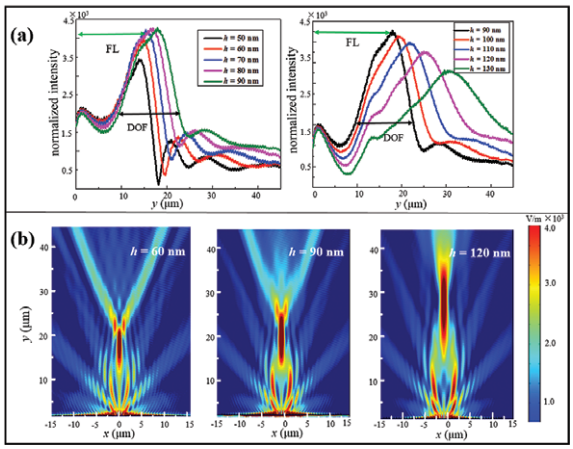

Fig. 5: (Colour online) (a) Intensity profiles of the proposed structure in the y-direction with different height h. (b) Electric-field intensity distribution with different distance $h = 50\,\text{nm}$, $90\,\text{nm}$ and $130\,\text{nm}$.

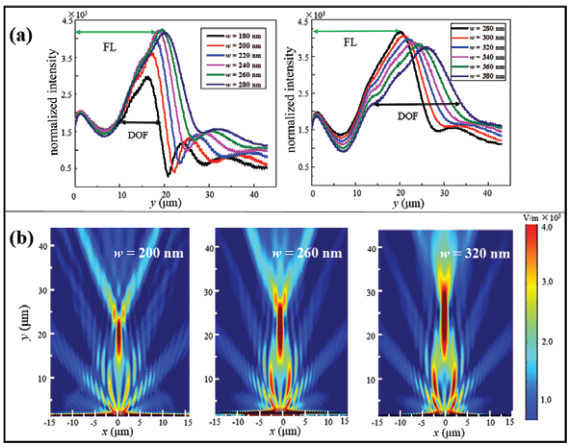

Fig. 6: (Colour online) (a) Intensity profiles of the proposed structure in the y-direction with different width w. (b) Electric-field intensity distribution with different width $w = 200\,\text{nm}$, $260\,\text{nm}$, and $320\,\text{nm}$.

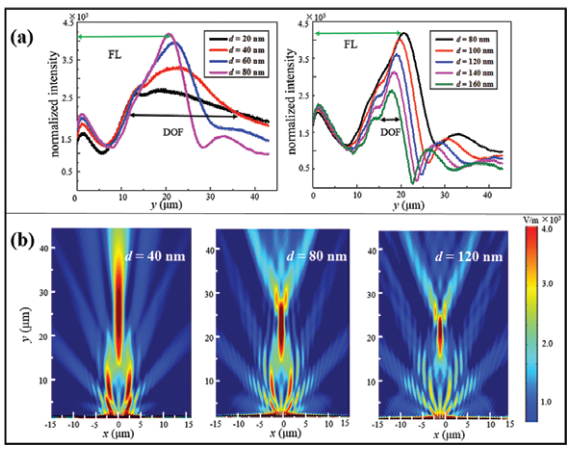

Fig. 7: (Colour online) (a) Electric-field intensity profiles of the proposed structure in the y-direction with different distance d. (b) Electric-field intensity distribution of the proposed structure with different distance $d = 40\,\text{nm}$, $80\,\text{nm}$, and $120\,\text{nm}$.

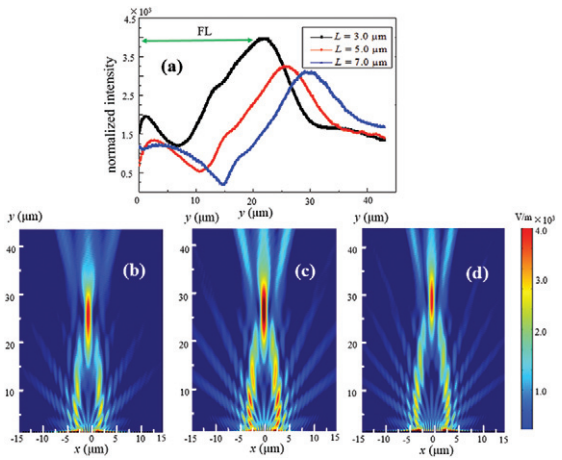

Fig. 8: (Colour online) (a) Electric intensity profiles of the proposed structure in the y-direction with different distance L. Electric intensity distribution of the proposed structure with different distance L; (b) $L = 4.0\,\mu\text{m}$, (c) $L = 5.0\,\mu\text{m}$, (d) $L = 6.0\,\mu\text{m}$.

increases, the DOF decreases, and as the scattering of the dielectric rectangles increases, the DOF increases.

The electric-field intensity profiles in the y-direction at different height h is shown in fig. 5(a). The electric-field intensity distribution with $h = 60$, 90, and 120 nm is shown in fig. 5(b). Results indicate that as the height h increases, the DOF increases. The cause of this increase is mainly that as the height h increases, the scattering of the dielectric rectangles increases, and the DOF increases. Thus, as the height h increases, so does the DOF.

The electric-field intensity profiles in the y-direction at different dielectric rectangle width w is shown in fig. 6(a). The electric-field intensity distribution with $w = 200$, 260, and 320 nm is shown in fig. 6(b). Results indicate that as the width w increases, the DOF also increases. The cause of this increase is mainly that as the width of dielectric rectangles increases, the scattering of the dielectric rectangles increases, and the DOF increases. Thus, as the height h increases, so does the DOF.

The electric-field intensity profiles in the y-direction at different distance d is shown in fig. 7(a). The electric-field intensity distribution with $d = 80$, 120, and 160 nm is shown in fig. 7(b). Results indicate that as the distance d increases, the DOF decreases. The cause of this increase is mainly that as the distance increases, the scattering of the dielectric rectangles decreases, and the DOF decreases. As d is larger than the penetration depth of SPPs, the program is close to SPPs for the air/metal interface. On the contrary, as d is very small, the program is close to SPPs for a dielectric/metal interface.

In addition, two extra observations in figs. 5–7 are that as the height h and the width w increase, the FL increases.

As the distance d increases, the FL decreases. Maximum electric-field intensity occurs around $w = 260\,\text{nm}$, $h = 90\,\text{nm}$, and $d = 80\,\text{nm}$. These results show that the FL and the maximum value of intensity can be controlled by simply choosing suitable rectangle sizes.

The intensity profiles of the electric field in the y-direction at different distance L is depicted in fig. 8(a). The black, red and blue graphs represent the intensity distribution with $L = 3.0$, 5.0, and $7.0\,\mu\text{m}$. The electric-field intensity distribution with different distances between two excitation slits, $L = 4.0$, 5.0, and $6.0\,\mu\text{m}$, is shown in figs. 8(b)–(d). An obvious observation is that, as the distance L increases, the position of the focusing spot moves away from the group of the dielectric rectangles. As the distance L increases, the DOF and the maximum value of intensity decrease in fig. 8(a). Because the mirror-symmetric spatial bending beams were obtained in the approximation limit (*i.e.*, $\theta < 20°$), and the approximation conditions cannot been matched at the top part of the target curve, hence the beam intensity decreases along the propagation direction.

Conclusions. – In conclusion, a double mirror-symmetric spatial bending beams generator was presented. The far-field focused beams were observed by the interference of the double mirror-symmetric spatial bending beams. A detailed comparison between the focusing properties of the proposed structure and the conventional monometallic grating was conducted. Results show that the depth of focusing, focusing length, and full width at half-maximum of the proposed structure were longer than those of the conventional structures. Moreover, the DOF of the proposed structure was two times longer than that of the conventional structures. The present study further demonstrated that the focusing properties of the proposed structure rely on the structural parameters of the dielectric rectangles, and on the distance between the dielectric rectangles and metal film. Finally, the position of the focusing spot was shown to have shifted and moved away from the bending beam generator. The authors believe that these findings offer potential applications in the field of sensors, optical tweezers, optical data storage, and photo-biomedical detection.

* * *

The work is financially supported by National Natural Science Foundation of China (NSFC) (Grant No. 61575117), the Fundamental Research Funds for the Central Universities of Ministry of Education of China (Grant Nos. GK201601008, GK201603015, and GK201604003).

REFERENCES

[1] Genet C. and Ebbesen T. W., *Nature*, **445** (2007) 39.
[2] Barnes W. L., Dereux A. and Ebbesen T. W., *Nature*, **424** (2003) 824.
[3] Brongersma M. L. and Shalaev V. M., *Science*, **328** (2010) 440.
[4] Jacob Z., Alekseyev L. V. and Narimanov E., *Opt. Express*, **14** (2006) 8247.
[5] Shao D. B. and Chen S. C., *Nano Lett.*, **6** (2006) 2279.
[6] Fletcher D. A., Crozier K. B., Quate C. F. *et al.*, *Appl. Phys. Lett.*, **77** (2000) 2109.
[7] Kennedy J. E., Wu F., Haar G. R. T. *et al.*, *Ultrasonics*, **42** (2004) 931.
[8] Zhao J., Ye H., Huang K. *et al.*, *Sci. Rep.*, **4** (2014) 6257.
[9] Ko H., Kim H. C. and Cheng M., *Appl. Opt.*, **49** (2010) 950.
[10] Verslegers L., Catrysse P. B., Yu Z. *et al.*, *Nano Lett.*, **9** (2008) 235.
[11] Verslegers L., Catrysse P. B., Yu Z. *et al.*, *Nano Lett.*, **9** (2008) 235.
[12] Liu Z., Steele J. M., Srituravanich W. *et al.*, *Nano Lett.*, **5** (2005) 1726.
[13] Zhang X., Yan L., Guo Y. *et al.*, *Plasmonics*, **11** (2016) 109.
[14] Ko H., Kim H. C. and Cheng M., *Appl. Opt.*, **49** (2010) 950.
[15] Kumar P., Tripathi V. K., Kumar A. *et al.*, *J. Appl. Phys.*, **117** (2015) 013103.
[16] Lin J., Dellinger J., Genevet P. *et al.*, *Phys. Rev. Lett.*, **109** (2012) 093904.
[17] Wei S., Lin J., Wang Q. *et al.*, *Opt. Lett.*, **38** (2013) 1182.
[18] Genevet P., Dellinger J., Blanchard R. *et al.*, *Opt. Express*, **21** (2013) 10295.
[19] Lin J., Mueller J. P. B., Wang Q. *et al.*, *Science*, **340** (2013) 331.
[20] Huang L., Chen X., Bai B. *et al.*, *Light Sci. Appl.*, **2** (2013) e70.
[21] Cao L., Li W., Wang Y. *et al.*, *IEEE Photon. Technol. Lett.*, **26** (2014) 1247.
[22] Min C., Shen Z., Shen J. *et al.*, *Nat. Commun.*, **4** (2013) 2891.
[23] Guan C., Ding M., Shi J. *et al.*, *Opt. Express*, **22** (2014) 18365.
[24] Li L., Li T., Wang S. M. *et al.*, *Phys. Rev. Lett.*, **110** (2013) 046807.
[25] Epstein I. and Arie A., *Opt. Lett.*, **39** (2014) 3165.
[26] Minovich A., Klein A. E., Janunts N. *et al.*, *Phys. Rev. Lett.*, **107** (2011) 116802.
[27] Salandrino A. and Christodoulides D. N., *Opt. Lett.*, **35** (2010) 2082.
[28] Tang X. M., Li L., Li T. *et al.*, *Opt. Lett.*, **38** (2013) 1733.
[29] Guan C., Ding M., Shi J. *et al.*, *Opt. Lett.*, **39** (2014) 1113.
[30] Li L., Li T., Wang S. M. *et al.*, *Phys. Rev. Lett.*, **107** (2011) 126804.
[31] Klein A. E., Minovich A., Steinert M. *et al.*, *Opt. Lett.*, **37** (2012) 3402.
[32] Epstein I. and Arie A., *Opt. Lett.*, **39** (2014) 3165.
[33] Li L., Li T., Tang X. M. *et al.*, *Light Sci. Appl.*, **4** (2015) 1001.
[34] Ordal M. A., Long L. L., Bell R. J. *et al.*, *Appl. Opt.*, **22** (1983) 1099.

[35] Aspnes D. E. and Theeten J. B., *J. Electrochem. Soc.*, **127** (1980) 1359.
[36] Li H., Xu Y., Wang G. *et al.*, *Opt. Commun.*, **383** (2017) 423.
[37] Liu Y., Zentgraf T., Bartal G. *et al.*, *Nano Lett.*, **10** (2010) 1991.
[38] Epstein I. and Arie A., *Phys. Rev. Lett.*, **112** (2014) 023903.
[39] Greenfield E., Segev M., Walasik W. *et al.*, *Phys. Rev. Lett.*, **106** (2011) 213902.
[40] Froehly L., Courvoisier F., Mathis A. *et al.*, *Opt. Express*, **19** (2011) 16455.